ACS NANO

www.acsnano.org

ARTICLE

Amphiphilic Particle-Stabilized Nanoliter Droplet Reactors with a Multimodal Portable Reader for Distributive Biomarker Quantification

Vishwesh Shah,◆ Xilin Yang,◆ Alyssa Arnheim, Shreya Udani, Derek Tseng, Yi Luo, Mengxing Ouyang, Ghulam Destgeer, Omai B. Garner, Hatice C. Koydemir, Aydogan Ozcan,* and Dino Di Carlo*

Cite This: *ACS Nano* 2023, 17, 19952−19960

Read Online

ACCESS | Metrics & More | Article Recommendations | Supporting Information

ABSTRACT: **Compartmentalization, leveraging microfluidics, enables highly sensitive assays, but the requirement for significant infrastructure for their design, build, and operation limits access. Multimaterial particle-based technologies thermodynamically stabilize monodisperse droplets as individual reaction compartments with simple liquid handling steps, precluding the need for expensive microfluidic equipment. Here, we further improve the accessibility of this lab on a particle technology to resource-limited settings by combining this assay system with a portable multimodal reader, thus enabling nanoliter droplet assays in an accessible platform. We show the utility of this platform in measuring N-terminal propeptide B-type natriuretic peptide (NT-proBNP), a heart failure biomarker, in complex medium and patient samples. We report a limit of detection of ∼0.05 ng/mL and a linear response between 0.2 and 2 ng/mL in spiked plasma samples. We also show that, owing to the plurality of measurements per sample, "swarm" sensing acquires better statistical quantitation with a portable reader. Monte Carlo simulations show the increasing capability of this platform to differentiate between negative and positive samples, i.e., below or above the clinical cutoff for acute heart failure (∼0.1 ng/mL), as a function of the number of particles measured. Our platform measurements correlate with gold standard ELISA measurement in cardiac patient samples, and achieve lower variation in measurement across samples compared to the standard well plate-based ELISA. Thus, we show the capabilities of a cost-effective droplet-reader system in accurately measuring biomarkers in nanoliter droplets for diseases that disproportionately affect underserved communities in resource-limited settings.**

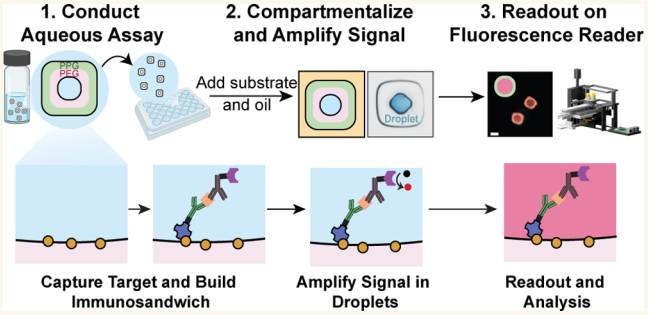

KEYWORDS: *droplet, low-cost sensors, ELISA, biomarker detection, portable reader, statistical quantitation*

The ability to compartmentalize reactions into extremely small volumes has enabled the study of biology with exquisite sensitivity.[1,2] Low/no crosstalk and uniformity ensure that each partition serves as an individual reaction compartment with comparable conditions. Currently available compartmentalization technologies, based on droplets or microwell arrays, require specialized infrastructure to operate.[3−5] Droplet assays are also marred by surfactant-induced diffusion of reaction products leading to crosstalk.[6] These limitations limit their accessibility and usability for diagnostics and research.

Previously, we described the production and use of multimaterial amphiphilic particles made of concentric hydrophobic and hydrophilic polymer layers to thermodynamically stabilize water-in-oil emulsions.[7,8] This lab on a particle method leverages the surface interactions of two different polymers to create a local energy minimum in the volume−energy curves, thereby stabilizing a fixed volume of the aqueous solution. This method of generating monodisperse reaction volumes with simple mixing steps democratizes sensitive droplet assays for use in life sciences research and

Received: June 3, 2023
Accepted: October 6, 2023
Published: October 12, 2023

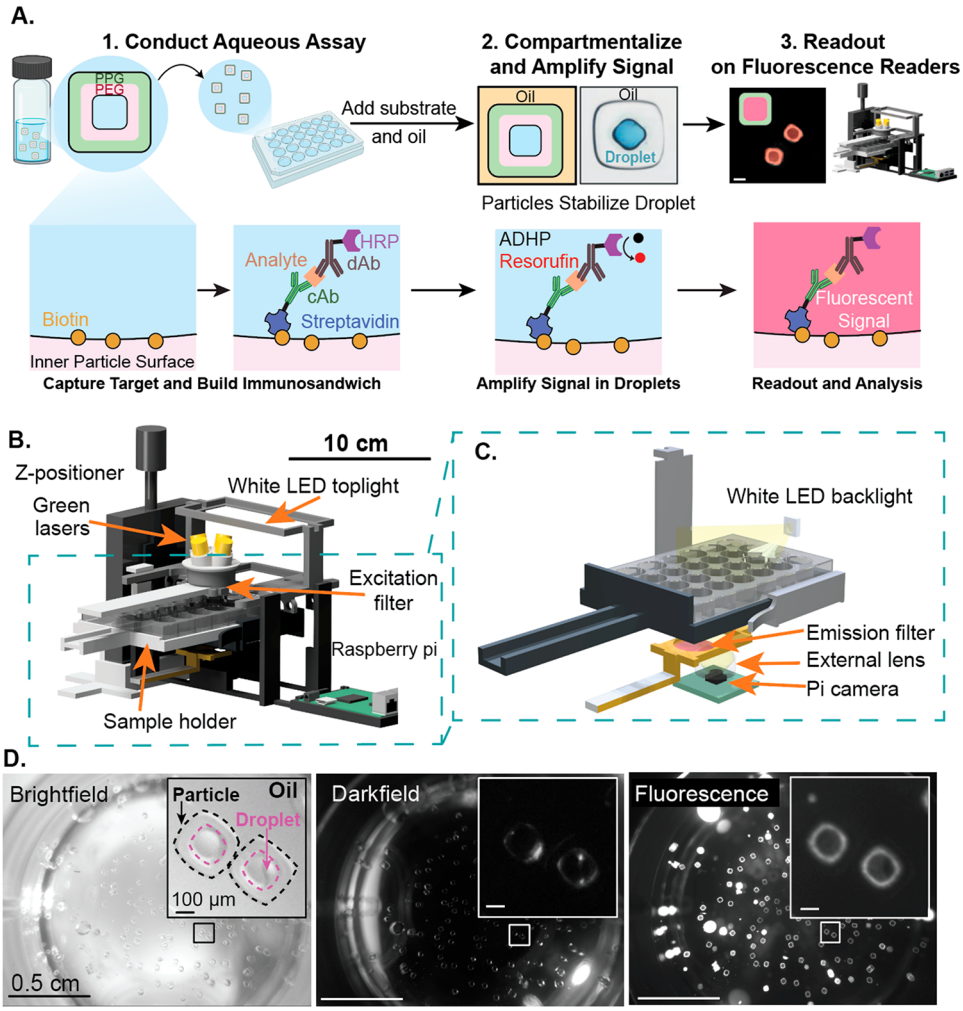

Figure 1. Amphiphilic particles workflow and portable reader design. (A) Schematic of the lab on a particle workflow for performing and reading out parallel amplified immunoassays in droplets. Initial steps to form an immunosandwich complex are similar to traditional particle/bead-based immunoassay platforms. After the final wash step, the enzyme substrate and oil are added in a quick sequence to isolate particle-templated droplets as individual reaction compartments. Fluorescence signal from enzymatic turnover of the ADHP substrate to resorufin quickly accumulates to detectable levels inside the small droplet volumes. The readout of each compartment is then conducted on a multimodal portable microscopic reader. (B) Multimodal reader design showing a Raspberry pi controlled automated camera for image acquisition, external lens capable of capturing the entire well field of view, excitation and emission filters for fluorescence acquisition, and LED backlights used for bright-field and dark-field illumination. (C) Magnified view of the imaging components of the reader showing laser diodes, emission filter, lens, and camera used to acquire images. (D) Representative bright-field, dark-field, and fluorescence images showing the whole well filled with particles following an assay (insert).

clinical diagnostics. Previous work, utilizing these particles with readout on benchtop inverted microscopes, reported limits of detection of N-terminal propeptide B-type natriuretic peptide (NT-proBNP), a canonical heart failure marker, down to femtogram per milliliter concentrations in buffer testing.[8]

The need for benchtop fluorescence and bright-field microscopes for end-point readout limits the deployment of this otherwise accessible technology in local clinics and resource-limited settings. Not surprisingly, the populations in these low-resource regions are often disproportionately affected by otherwise preventable medical conditions and could benefit from technologies for sensitive and quantitative biomarker detection. For example, historical and ongoing evidence shows that heart failure (HF) disproportionately negatively affects underserved populations in economically deprived regions often comprising of minority populations.[9−12] The Multi-Ethnic Study of Atherosclerosis found that African American and Hispanic populations in the United States had the highest risk of developing HF, and African Americans had the highest proportion of incident HF not preceded by myocardial infarction (75%).[13] While HF is treatable upon diagnosis, a recent study found that ∼80% of patients are only diagnosed upon emergency hospital admission.[14] AHA guidelines establish the measurement of NT-proBNP for the diagnosis of HF with a clinical cutoff of 0.125 ng/mL.[15] Results from the Heart Failure Assessment With BNP in the Home (HABIT) showed that B-type Natriuretic Peptide (BNP) levels, monitored as a continuous variable over time, can be correlated to the risk of a patient experiencing acute clinical heart failure decompensation (ADHF),[16] and thus can help reduce 30 day emergency hospital readmission rates. Improving access to NT-proBNP testing at local clinics and other outpatient settings can help detect HF before emergency hospital admission and improve patient outcomes, especially in underserved communities.

https://doi.org/10.1021/acsnano.3c04994
ACS Nano 2023, 17, 19952−19960

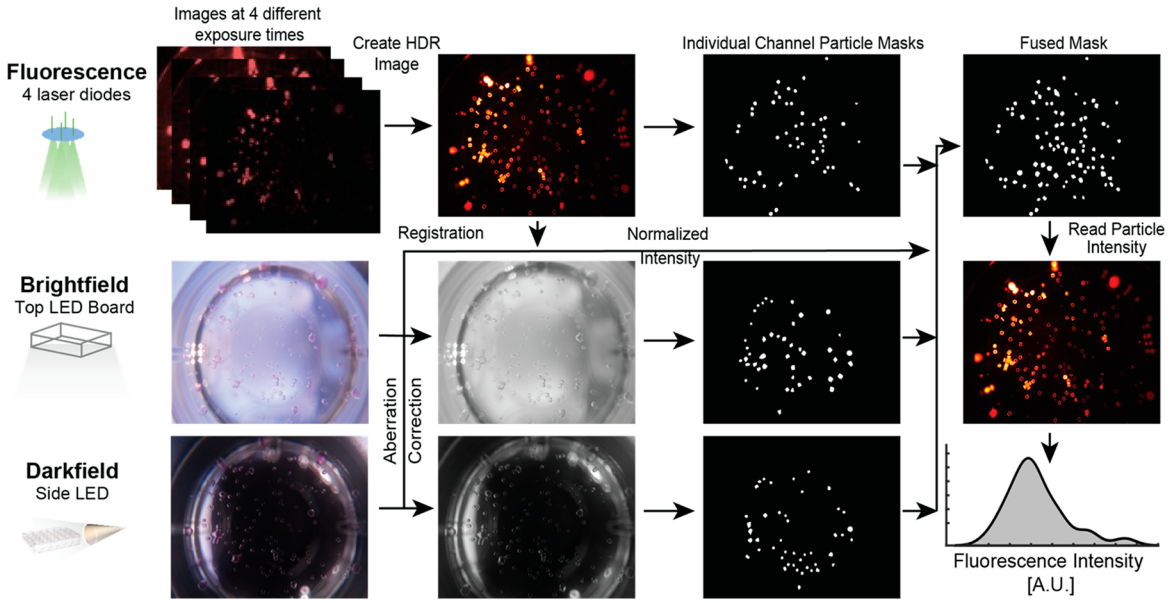

Figure 2. Image processing workflow. Fluorescence, bright-field, and dark-field images are captured following illumination with laser diodes, a top LED board, and side LEDs, respectively. All acquired images are then fed into a customized image processing algorithm and fluorescence intensity measurements associated with each detected particle are returned. A preprocessing module first synthesizes the high-dynamic range (HDR) image, corrects the chromatic aberration, and registers images from the first three modalities. Then, for each modality, an edge detector based algorithm extracts the regions of interest (ROI) containing particles and generates binary masks for the particles. Three binary particle masks are fused together through OR operations and the fluorescence intensities of each particle from the HDR image is assigned to each region of interest. The histogram shows the kernel density of fluorescence intensities from a population of particles.

Here, we present a cost-effective laboratory-on-a-particle based assay and develop a portable reader and algorithm to measure NT-proBNP levels in plasma-EDTA and patient samples. The microparticle-based assay achieves amplified sensing in tens to hundreds of individual compartmentalized reaction volumes simultaneously, resulting in enhanced performance through increased statistical sampling, and follows a simple workflow. The portable, low-cost reader has a small footprint (10 in. × 8 in.) and can be placed in local clinics and remote health centers. The images generated for an entire reaction well are analyzed by the portable reader to detect each particle and the reaction occurring within the enclosed droplets. Leveraging this platform, we show ratiometric response to increasing doses of NT-proBNP spiked into plasma-EDTA sample and a correlated measurement between this platform and standard well plate ELISA in cardiac patient samples. We conducted Monte Carlo simulations showing the decreasing error rates in measurements, increasing capability to distinguish between samples at and above the clinical cutoff for acute heart failure (0.1 ng/mL) and those below as a function of the number of simultaneous particle measurements obtained from each sample.

RESULTS AND DISCUSSION

Amphiphilic Lab-on-a-Particle ELISA. The assay uses multimaterial particles (~300 μm in diameter) with concentric layers of an inner polyethylene glycol (PEG) layer and an outer polypropylene glycol (PPG) layer with a cavity in the middle (Figure 1a), which allows them to hold a small aqueous reaction volume. Particles were fabricated using 3D-printed microfluidic devices that are smaller and redesigned structurally (Supplementary Figure 1) for more streamlined fabrication compared to those previously described, possible by advances in micro-stereolithography.[8,17] During fabrication, the inner PEG region was functionalized with biotin to enable linking to streptavidin-conjugated capture antibodies with an affinity to the target analyte. The assay format uses a standard ELISA sandwich with horseradish peroxidase-conjugated detector antibodies used to turnover a fluorogenic enzyme substrate in the reaction volume and accumulate fluorescent products (Figure 1a). The compartments are formed spontaneously through the addition of oil to the amphiphilic particles.[7,18] The inner PEG region stabilized a nanoliter droplet in which the enzyme-catalyzed fluorescent product of the ADHP substrate is quickly concentrated to detectable levels.

Portable Reader and Image Processing Workflow. We designed a portable, low-cost, multimodal reader to facilitate the readout from the assay (Figure 1b). The reader has a small footprint (10 in. × 8 in.) and consists of a z-positioning stage to focus sample, sample holder, Raspberry Pi-based controller, and an imaging module. The imaging module comprises 4 green (532 nm) laser diodes to excite fluorophores (570 nm peak), top white light-emitting diodes (LED) for bright-field imaging, and a side angle LED for dark-field imaging (Figure 1c). The images are captured with and without an insertable emission filter (used for fluorescence imaging), an external lens, and a Raspberry Pi camera. The magnification of the optical system, ~0.2×, was designed to take whole well images in bright-field, dark-field, and fluorescence modalities (Figure 1d and "Methods" section).

We also developed an image processing pipeline (Figure 2) to automate microparticle detection and the fluorescence intensity measurement for each droplet from captured images. We first created a high dynamic range (HDR) image from four individual low dynamic range (LDR) images. We then corrected the chromatic aberrations on bright-field and dark-

https://doi.org/10.1021/acsnano.3c04994
ACS Nano 2023, 17, 19952−19960

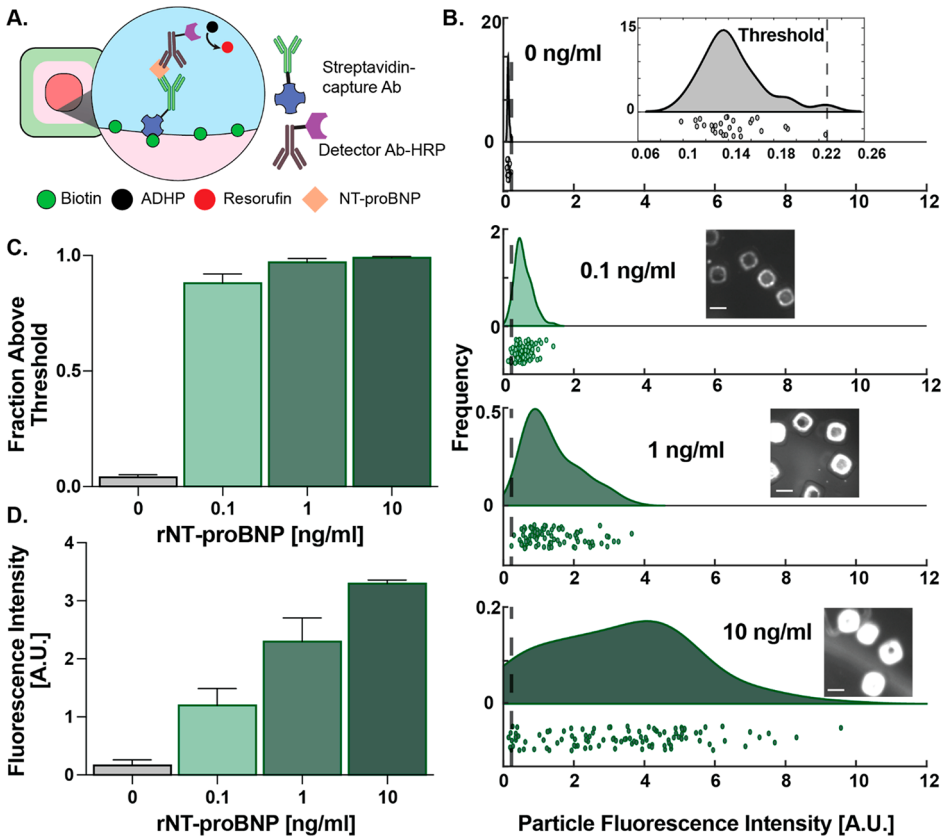

Figure 3. NT-proBNP detection in buffer. (A) Schematic showing immunosandwich formation for NT-proBNP detection on the inner particle surface. (B) Rain-cloud plots showing distribution of fluorescence intensities of individual particles with increasing spiked NT-proBNP levels. Top inset shows threshold determination as $\mu_0 + 3\sigma_0$, and other insets show images of fluorescence signals in particle-droplets at respective concentrations. Scale bar is 100 μm. (C) Mean fraction of particles above threshold. Error bars show the standard deviation. (D) Mean particle intensities from three experimental repeats.

field images and registered them to form a synthesized HDR image. A customized particle detection algorithm was applied to registered images for each modality individually, creating three binary masks which were then fused to one final detection mask. We noticed that due to the variations in lighting conditions in the different images taken of the same well, the algorithm detected different fractions of particles with each imaging mode (Supplementary Figure 2). On average, the algorithm detected 24% of the particles from the bright-field image, 21% from the dark-field image and 56% from the HDR fluorescence image. The detectable percentage for HDR images was lower when the sample's fluorescence signal was lower and vice versa. Combining masks from each individual bright-field, dark-field, and fluorescence images led to a majority of particles being detected, providing more measurements per sample. Each unconnected region of interest (ROI) was considered a single particle, and the fluorescence intensity profile was measured by overlaying the masks on the HDR image. Detecting from three modalities increased the number of particles that could be analyzed, which can increase the accuracy and robustness of our system as described below, especially when fluorescence signals were low and contained insufficient information for detection. Due to a large number of particles initially seeded into a well (~150), 100% particle detection accuracy is not needed for a successful assay readout.

NT-proBNP Detection Using Amphiphilic Particles and Portable Reader. We first developed image analysis procedures for the combined assay and reader that maximized the capability to measure NT-proBNP levels above and below the clinically relevant cutoff (~0.1 ng/mL) concentration in buffer. We identified 3 potential regions of interest (ROIs) within a particle-droplet compartment to quantify fluorescence intensity (Supplementary Figure 3): the inner PEG region, the droplet region, or the union of both the PEG and droplet regions (combined ROI). We found that the droplet region had the lowest fluorescence intensity out of the three ROIs and observed that resorufin, the fluorescent product of the enzyme-catalyzed oxidation of ADHP, appeared to accumulate or have higher fluorescence intensity in the PEG region. The PEG ROI and combined ROI had similar fluorescence intensities at 0.1 ng/mL (Supplementary Figure 2), however using the combined ROI we were able to achieve higher statistical significance, p-value 10^{-11} versus 3×10^{-9}, between the fluorescence intensity distributions of a negative control (0 ng/mL) and 0.1 ng/mL sample (Supplementary Figure 3). As such, we used the combined ROI for all subsequent experimental analysis.

After establishing image analysis protocols, we characterized the assay performance by spiking various concentrations of NT-proBNP in buffer. Leveraging the ability to achieve multiple measurements per sample across an assembly of separate particles we could increase overall measurement accuracy, a process referred to as "swarm sensing".[19] On average, we measured intensities from 80 particles per sample. Based on the distributions of fluorescence intensities of a negative control, we set a threshold of mean +3× of the

https://doi.org/10.1021/acsnano.3c04994
ACS Nano 2023, 17, 19952−19960

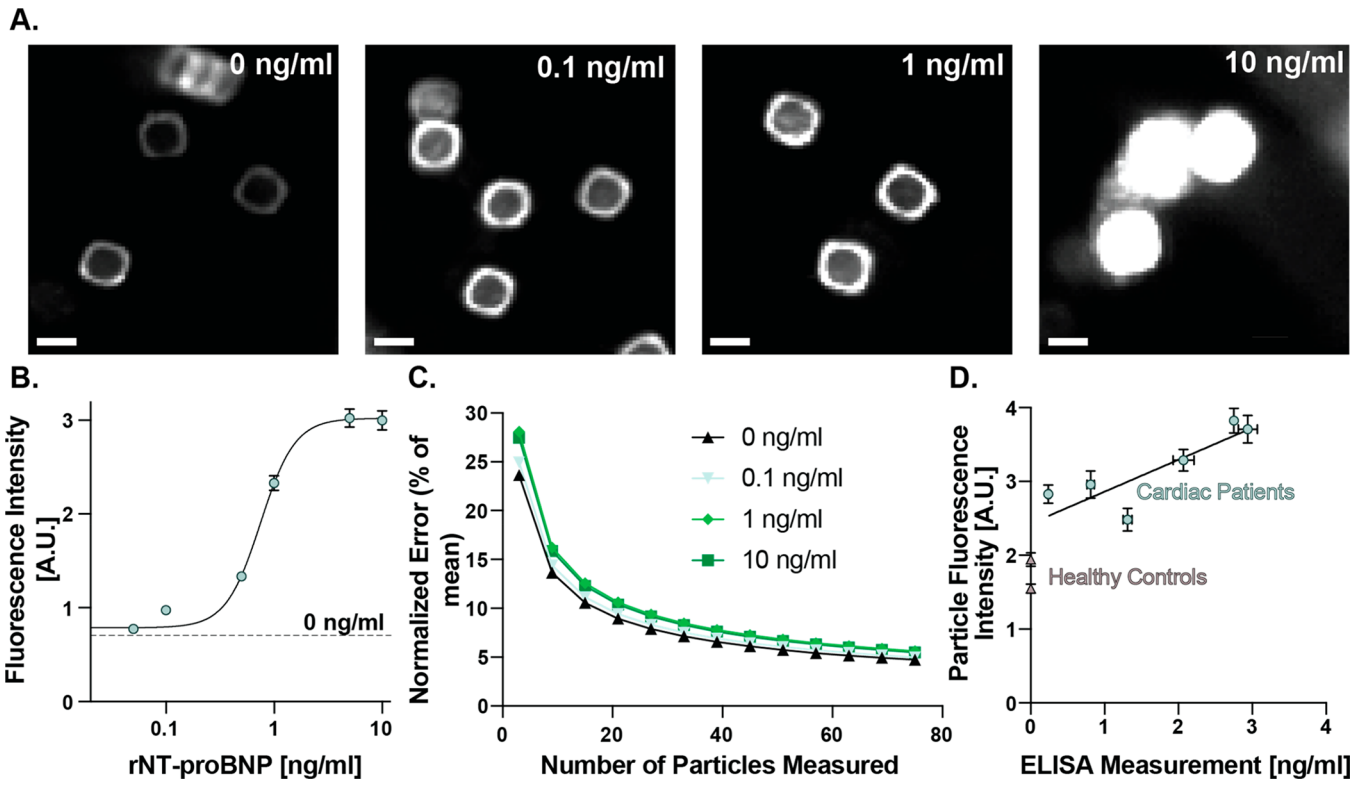

Figure 4. Plasma-EDTA spiked and patient testing. (A) HDR images showing concentration dependent response in fluorescence intensity. (B) Mean fluorescence intensities across 3 experimental repeats and >250 particle-droplets. (C) Standard error of the mean as a function of measurements taken per sample under varying conditions. (D) Measurements of cardiac patient samples using a particle-portable reader system (*y*-axis) versus standard well plate based ELISA (*x*-axis). Control samples were below the quantitation threshold of the ELISA (<15 pg/mL).

standard deviation ($\mu_{\text{negative-control}} + 3\sigma_{\text{negative-control}}$) (Figure 3b inset). We then calculated the fraction of total particles detected with fluorescence intensities above this threshold for each NT-proBNP spiking concentration of 0.1, 1, and 10 ng/mL (Figure 3b). Across three repeats of this experiment, we found that the assay showed a step response, where the mean fraction above the threshold was close to zero (0.025) for 0 ng/mL and was saturated at ∼1 for 0.1, 1, and 10 ng/mL, accounting for variations across the experimental repeats (Figure 3c). The mean fluorescence intensity of the distributions across experimental repeats showed dose−response-type behavior with a linearly increasing mean fluorescence intensity with increasing NT-proBNP concentrations (Figure 3d). Overall, the assay was able to distinguish between the clinical cutoff at 0.1 ng/mL and negative control (0 ng/mL), with linearity in fluorescence intensities helping quantitate across a concentration range that is clinically meaningful for improved age-adjusted positive predive value (PPV) (0.45−1.8 ng/mL) for HF.[20−22]

Next, we sought to assess assay performance in a complex medium. We spiked NT-proBNP in plasma-EDTA samples previously depleted of endogenous NT-proBNP (<15 pg/mL) and diluted spiked plasma in buffer at a ratio of 1:3 to reduce matrix effects. The spiked samples were tested using the lab on a particle assay and analyzed by the portable reader. We noticed a correlated increase in fluorescence intensity with increasing spiked NT-proBNP (Figure 4a,b; Supplementary Figure 4), with a linear response between 0.2−2 ng/mL and limit of detection (LOD) at 50 pg/mL (Figure 4b). Each individual particle-droplet provided an individual measurement, providing ∼80 measurements per sample; this multiplicity in measurement helps overcome random errors and improves quantitation with a low-cost reader. When the number of particles measured is increased from 3−80, the standard error of the mean for each measurement decreases from ∼27% to <5% (Figure 4c), lowering error 5-fold on average across conditions.

To better understand the diagnostic impact of multiple measurements of the same sample by multiple amphiphilic particles, we conducted Monte Carlo simulations to understand the error rate of designating a sample as positive or negative based on counting the number of particles above a threshold set by the distribution of negative control particle intensities (Supplementary Figure 5). In our analysis, we found that based on this thresholding method, the negative control sample had no particles above the threshold and was always designated as a negative. However, the sample at the clinical cutoff (0.1 ng/mL), showed a large variation (Supplementary Figure 5a) based on the number of particles analyzed for that sample. As the number of measurements per sample increased, the error rate of designating a sample as false negative exponentially decreased, i.e., the ability of this low-cost system to correctly identify a sample at the cutoff as being positive asymptotically increased with the increasing number of particles measured. Across three experimental repeats (Supplementary Figure 5b), we found that this thresholding method could easily differentiate between samples at or above the clinical cutoff (0.1−10 ng/mL) and those below (0, 0.05 ng/mL). This ability to obtain tens of measurements per sample and generate thresholds or summary statistics is a

https://doi.org/10.1021/acsnano.3c04994
ACS Nano 2023, 17, 19952−19960

particular advantage of our particle-based assay system, which helps improve quantitative capabilities with a low-cost reader.

To confirm that our system benefitted from this thresholding method, we expanded upon the analysis conducted in Figure 3c,d, focusing on the repeats conducted in spiked serum samples (Supplementary Figure 6). We compare two distinct approaches: the "Fraction Above Threshold" method and the utilization of "Mean Intensity" measurements derived from the intensities of all particles. The "Fraction Above Threshold" approach consistently offers a clear background signal, often reducing the negative control to either zero or a minimal value. This facilitates differentiation between the negative control and samples with a concentration of 0.1 ng/mL. In contrast, when using raw fluorescence intensity measurements, challenges in interpretation arise due to variable background signals. This variability complicates the establishment of a reliable threshold for distinguishing between the negative control and the 0.1 ng/mL samples. We conducted a single-tailed t test to assess the comparative effectiveness of the "Fraction Above Threshold" method and the "Mean Intensity" method in distinguishing between negative control and 0.1 ng/mL samples. Our analysis was based on the distribution of measured values obtained from three repetitions for each method. The outcome was a lower p-value (2.3×10^{-4}) for the "Fraction Above Threshold" method, in contrast to the much higher p-value of 0.1834 for the "Mean Intensity" method. These findings demonstrate compelling statistical evidence that strongly supports the superior performance of the "Fraction Above Threshold" method in this application.

Following the serum characterization, we performed testing on a small pool of patient samples for which we had gold standard NT-proBNP levels by standard plate ELISA (Supplementary Figure 7). The patient samples were well characterized by a gold standard ELISA measurement (limit of detection: 11.5 pg/mL; limit of quantification 21.9 pg/mL), showing a low variation over 2 and 4-fold dilution curves (Supplementary Figure 7a), with NT-proBNP concentrations ranging from 0.236−2.9 ng/mL. The particle and portable reader system results were well correlated with those of the ELISA measurements (Figure 4d), showing a linear correlation between the two measurements. Again, owing to the "swarm" sensing mechanism, the particle and portable reader system was able to achieve lower variations in measurements across the six patient samples (∼5%) compared to the standard ELISA for the same patient samples (∼9%) (Supplementary Figure 5d) readout on a standard plate reader.

STUDY LIMITATIONS

While this study was able to achieve detection capabilities in clinically relevant ranges, we did not assess the effect of parameters such as various incubation times on resolving capabilities of the assay. Signal amplification time is particularly important since ADHP continuously converts to resorufin, boosting the overall fluorescence signal within aqueous droplets. Our initial studies with these amphiphilic particles explored incubation time's impact on signal development, showing significant differences between high and low HRP concentration particles.[8] However, as time progresses, fluorescent resorufin diffuses to adjacent droplets, especially during overnight incubation. We selected a 60 min incubation time based on this previous research, which found that a 45−60 min incubation was sufficient to see signal differentiation between high and low HRP concentrations, but not long enough to see crosstalk to negative particles.[8,17] Further studies could optimize the incubation time for signal development while balancing signal amplification and crosstalk concerns.

In this study, we also implemented an image processing workflow that was off the portable reader, requiring data export to, and processing on, a separate machine. While this reduces accessibility, it is imperative to emphasize the potential merits of cloud-based computation. Raspberry Pi's integrated Wi-Fi module enables the seamless data transmission to cloud infrastructures for subsequent analysis and archival. This approach would send the captured data to the cloud for analysis and storage, potentially allowing for more robust processing and improved data security. Nonetheless, localized processing, i.e., processing on the reader, is still viable by transferring the processing pipeline directly to the Raspberry Pi. This can be efficiently achieved by leveraging open-source libraries such as OpenCV paired with Python.

CONCLUSION

Compartmentalized assays leverage small volumes to achieve higher sensitivity; however, they require significant infrastructure. Our amphiphilic particles can thermodynamically stabilize nanoliter droplets as reaction compartments, foregoing the need for expensive equipment to form droplets or fill microchambers and realizing compartmentalized assays in an accessible well plate format. Here, we combined this technology with a low-cost portable reader and image analysis algorithm to potentially extend the access of this technology for distributed use in local laboratories and clinics. We demonstrated the ability of this combined assay-reader system to measure NT-proBNP levels, a canonical heart failure marker, in complex media and patient samples. From the plurality of particles added per well, we were able to obtain tens of measurements per sample, thereby improving quantitation capabilities and reducing measurement error from using a low-cost imaging system. Particle numbers can also be adjusted depending on the application and sensitivity requirements. In the future, we can also combine this with different shapes of particles to barcode each patient or biomarker and enable patient pooling or multiplexed analyte panel testing for scaling and further lowering cost per patient per analyte. Even though this version of this particle-reader platform is not amenable for at-home testing, through our work we have been able to show the following: (1) improved accessibility of compartmentalized assays beyond the needs for highly specialized infrastructure and (2) through future multiplexing capabilities reduction in per patient costs of conducting large scale tests. Computer vision algorithms can also help detect these barcodes from a single white light image, enabling barcoded droplet assays in an easily deployed format. In conclusion, this platform potentiates the nanoliter droplet assay for screening and monitoring, thereby enabling earlier detection and quicker treatment/intervention decision times in low-resource settings.

METHODS

Particle Fabrication and Functionalization. Coaxial flow lithography was implemented to fabricate amphiphilic particles using an improved 3D printed device design that is 3.5× smaller by volume than the previously reported devices, possible by advances in microstoichiography (Boston Microfabrication). The updated design also features angled, rather than perpendicular connections between inlets and internal channels, which along with the smaller channel

https://doi.org/10.1021/acsnano.3c04994
ACS Nano 2023, 17, 19952−19960

dimensions decreases the chance of air bubbles being entrapped which would previously often lead to flow profile deformations (Supplementary Figure 1). As previously reported,[17] we flowed four precursor solutions through the concentric channels to obtain coaxial flows as follows from outer to inner stream: (1) inert sheath of poly(propylene glycol) [PPG], (2) poly(propylene glycol) diacrylate [PPGDA] + photo initiator, (3) poly(ethylene glycol) diacrylate [PEGDA] + acrylate-PEG-Biotin + photo initiator, and (4) inert sheath of poly(ethylene glycol) [PEG]. These precursor streams were run at a total flow rate of 1−2 mL/min, with flow rate ratios of 1:1 and 2:1 (PPG/PPGDA: PEGDA/PEG). Once the coaxial flow is created, we polymerized the reactive streams using UV light exposed through patterned slits (70−100 μm) in a photomask for a short duration (450−700 ms) to obtain particles with defined 3D geometries. We can fabricate 100−120 particles per cycle depending on the exposed region size. After fabrication, the remaining precursor material is washed away from particles by dilution using ethanol. Particles are stored in ethanol at 4 °C before use.

Amphiphilic Particle Assay. We first transferred biotinylated particles suspended in ethanol to a 24-well plate and counted them to ensure a similar distribution per well. Following the transfer, we washed the particles with PBSP (PBS with 0.5% w/v Pluronic F-127) before incubating with 10 μg mL^{-1} streptavidin (ThermoFisher Scientific) for 30 min. After incubation, we washed the particles with PBSP and incubated them with 10 μg mL^{-1} capture antibody (15C4 cm^3, HyTest) solution. Following another round of washing, we blocked the particle and plate surface using a protein-free blocking buffer (ThermoFisher Scientific) for 1 h.

We incubated functionalized particles with samples, NT-proBNP (HyTest) at desired concentrations spiked in buffer, or NT-proBNP free plasma-EDTA (HyTest). Control samples were incubated with only buffer or NT-proBNP free plasma. Following incubation with the antigen, we washed particles with a 0.05% Tween 20 solution to remove the unbound antigens. We then incubated for an hour with 1.5 μg mL^{-1} HRP-conjugated detection antibody (13G12 cm^3, HyTest) in BSA buffer (PBS with 0.1% w/v BSA) and washed. For the signal generation, we added a QuantaRed assay solution (ThermoFisher) to the particles and immediately removed them and added PSDS oil (Sigma-Aldrich) to form aqueous droplets stabilized within the particles. The particles were incubated for signal development before imaging using a portable reader. We captured bright-field, dark-field, and four fluorescence images (at 100, 500, 1000, and 2000 ms exposure) of each well.

During this developmental process, we utilized particles from various batches that were manufactured over a 12 month period (2020−2021). Each batch was used for a complete set of experiments. We note the robustness of the assay-reader platform given that we were able to achieve consistent results across different particle batches made 2−3 years ago. This also shows the robustness and shelf life of the amphiphilic particles under storage at 4 °C.

Portable Imager. The customized reader consisted of three major compartments: an illumination module, an imaging module, and a sample holder module. The illumination module had three independent illumination sources: a top white LED board (Adafruit White LED Module, ID1622), four laser diodes (Q-BAIHE, Industrial Green Laser, 532MD-100-HS-GD) with a diffuser, and a white LED (SunLED XSFWCB983W-ND). The white LED board provided uniform white illumination for bright-field imaging. The side-diffused LED was placed so that the sensor was close but perpendicular to the light path. With the presence of the sample, some part of the illumination was scattered by the particles into the sensor, emphasizing the high-frequency signal, i.e., the PEG layer of the particles, while reducing the background. The four laser diodes were installed 15° off the vertical axis, and the focusing lenses were removed to form four uniform light cones, creating four overlaid elliptical light spots for a uniform illumination covering the entire well. The imaging module included a Raspberry Pi camera module with an embedded Sony IMX219 sensor, an external lens, and an insertable band-pass filter (Edmund Optics 625 nm CWL, OD 4.0 25 nm Bandpass Filter) to filter out the excitation light for the fluorescent channel. The sample holder module consisted of a z-positional stage for focusing and a sliding sample holder. Illumination sources and image acquisition were fully powered and controlled by a Raspberry Pi with a customized Graphical User Interface (GUI), except for the laser diodes, which were powered by an external source. We applied heat paste around the laser diodes to avoid laser overheating. All holders for illumination and the sample well plate were customized and 3D-printed (Objet30 Pro, Stratasys, Ltd.) The fluorescence images were read directly from the sensor in a raw format. The raw format files are decoded and demosaiced to extract only the red channel. This process removed the redundant in-device preprocessing and reduced the laser operating time by ∼3-fold. Using raw images for fluorescence channels also improved the dynamic range of the sensor from 8-bit depth to 10-bit depth. Note that 8-bit fluorescence images suffer from several under- and overexposure problems, and for 10-bit images, the information loss was less significant but still occurred at negative control and 10 ng/mL concentrations.

Image Acquisition. For each experiment, we first previewed the field-of-view using the bright-field channel and manually focused the images with the z-stage. We then captured fluorescence, bright-field, and dark-field images using four green laser diodes with a diffuser, top board white LED, and side LED as light sources, respectively. Four fluorescence images of each field-of-view were acquired with exposure times of 100, 500, 1000, and 2000 ms, where 2000 ms was the maximum exposure time of the sensor. All four fluorescence images were registered and used to generate the HDR image. The exposure time for bright-field and dark-field images was 50 ms. All image sizes are 3280 × 2464 pixels.

Image Processing. Fluorescence images with different exposure times were registered using phase correlation[23] to correct possible shifts among the images. A Gaussian-weighted HDR algorithm was then applied to synthesize the HDR image from LDR images.[24] The bright-field and dark-field images were converted to grayscale and corrected to minimize the effects of chromatic aberration with empirical second-order parameters. Then the corrected images were registered to the HDR image using the rigid phase correlation method.[25] We then preprocessed the bright-field and dark-field images using adaptive histogram equalization[26] and bilateral Gaussian filtering[27] to enhance the contrast and reduce noise while preserving the edges. To detect particles from images, we utilized a Canny edge detector to extract the particle boundaries.[28] Image dilation was then applied to binary images from the Canny detector, and morphological processing was utilized to fill the holes in the images and generate masks for particles. Each unconnected mask represented a potential detected region of interest (ROI) for a particle but included false positive detections. False positive masks were filtered out based on their area (size) and eccentricity (shape) with empirical thresholds. Overlapped particles and particles near the edge of the well were excluded. This detection process was fine-tuned and applied to each modality individually. Then the three binary masks were fused together with a convexity constraint. The fused mask was superimposed on an HDR image to define the ROI, and fluorescence intensities from these ROIs were measured.

All the image processing algorithms employed utilize standard functions within MATLAB's Image Processing Toolbox. The processing procedures from raw measurements can be executed in less than 10 s in a standard personal laptop (Intel i9−11980HK central processing unit with 32 GB random access memory), even in the absence of any specific optimizations for speed.

Our image processing workflow detected all possible particles in all three different modalities. The algorithm was filtered based on intensity and shape to remove false detections such as overlapping particles, those oriented with their side facing up, and weak reflections. For the final prediction, we incorporated the intensity measurements from all detectable particles, meaning we do not confine ourselves to a fixed number of particles for each well.

ELISA Testing. To determine the gold standard NT-proBNP concentrations, we performed ELISA on patient samples using a kit (Abcam ab263877). The kit included a 96-well plate with capture

https://doi.org/10.1021/acsnano.3c04994
ACS Nano 2023, 17, 19952−19960

antibodies prebound to each well. Patient serum samples were analyzed whole, half-diluted, and quarter-diluted. After incubation with both patient samples and then detection antibodies, the colorimetric optical density readout was done at 450 nm on a microplate reader.

Monte Carlo Swarm Sensing Simulations. To study the effects of the number of particles detected on NT-proBNP quantification, we applied Monte Carlo simulation to evaluate the variation and robustness of the measurements. We first randomly selected an experiment from the serum sample and extracted the intensities profiles of all detected particles for negative control (0 pg/mL) and clinical cutoff (100 pg/mL). Then we randomly sampled a subset of all intensities (from 1 to 50 particles) for both concentrations. For the selected intensities, we measured the mean intensity for each concentration and calculated the *p*-value for a single-tailed *t* test and fraction above threshold. The random sampling was repeated 5000 times with a uniform probability for each particle, and we measured the mean and standard deviation for all three metrics across the repeats.

ASSOCIATED CONTENT

Supporting Information

The Supporting Information is available free of charge at https://pubs.acs.org/doi/10.1021/acsnano.3c04994.

cost breakdown of the portable image reader; comparisons between the old and updated 3D printed coaxial flow fabrication device; data on image analysis algorithm development including particle recognition and region of interest; full distribution of particle intensities as a function of analyte concentration; "swarm" sensing analyses; comparisons between fraction above threshold and mean intensity analyses; patient samples characterization (PDF)

AUTHOR INFORMATION

Corresponding Authors

Dino Di Carlo − *Department of Bioengineering, University of California - Los Angeles, Los Angeles, California 90095, United States; California Nanosystems Institute (CNSI), University of California - Los Angeles, Los Angeles, California 90095, United States;* orcid.org/0000-0003-3942-4284; Email: dicarlo@ucla.edu

Aydogan Ozcan − *Department of Electrical and Computer Engineering and California Nanosystems Institute (CNSI), University of California - Los Angeles, Los Angeles, California 90095, United States;* orcid.org/0000-0002-0717-683X; Email: ozcan@ucla.edu

Authors

Vishwesh Shah − *Department of Bioengineering, University of California - Los Angeles, Los Angeles, California 90095, United States;* orcid.org/0009-0006-8026-1260

Xilin Yang − *Department of Electrical and Computer Engineering, University of California - Los Angeles, Los Angeles, California 90095, United States*

Alyssa Arnheim − *Department of Bioengineering, University of California - Los Angeles, Los Angeles, California 90095, United States*

Shreya Udani − *Department of Bioengineering, University of California - Los Angeles, Los Angeles, California 90095, United States*

Derek Tseng − *Department of Electrical and Computer Engineering, University of California - Los Angeles, Los Angeles, California 90095, United States*

Yi Luo − *Department of Electrical and Computer Engineering, University of California - Los Angeles, Los Angeles, California 90095, United States;* orcid.org/0000-0001-9442-547X

Mengxing Ouyang − *Department of Bioengineering, University of California - Los Angeles, Los Angeles, California 90095, United States;* orcid.org/0000-0002-7824-617X

Ghulam Destgeer − *Department of Electrical Engineering, Technical University of Munich, Munich 80333, Germany*

Omai B. Garner − *Department of Pathology and Laboratory Medicine, University of California - Los Angeles, Los Angeles, California 90095, United States*

Hatice C. Koydemir − *Center for Remote Health Technologies and Systems, Texas A&M Engineering Experiment Station, College Station, Texas 77843, United States; Department of Biomedical Engineering, Texas A&M University, College Station, Texas 77843, United States*

Complete contact information is available at: https://pubs.acs.org/10.1021/acsnano.3c04994

Author Contributions

◆V.S. and X.Y. contributed equally to this work. V.S., X.Y., M.O., H.C.K., O.G., A. O., and D.D. conceived the idea and contributed to the design of experiments. V.S., X.Y., A.A., and S.U. conducted experiments. V.S., X.Y., D.T., Y. L., H.C.K., and A.O. guided reader design and troubleshooting. V.S., A.A., G.D., M.O., S.U., and D.D. guided assay design and troubleshooting. V.S. and X.Y. processed data. V.S., X.Y., A.A., and D.D. drafted the manuscript, and all authors provided feedback.

Notes

This work has been previously submitted to a preprint server: Shah, V.; Yang, Y.; Arnheim, A.; Udani, S.; Tseng, D.; Luo, Y.; Ouyang, M.; Destgeer, G.; Garner, O.; Kodemir, H. et al. Amphiphilic Particle-Stabilized Nanoliter Droplet Reactors With aMulti-Modal Portable Reader for Distributive Biomarker Quantification. *bioRxiv (Bioengineering)*, September 27, 2023, 2023.04.24.538181, ver. 1. DOI: 10.1101/2023.04.24.538181.

The authors declare no competing financial interest.

ACKNOWLEDGMENTS

The authors acknowledge the National Science Foundation PATHS-UP Engineering Research Center (Grant No. 1648451).

REFERENCES

(1) Basu, A. S. Digital Assays Part I: Partitioning Statistics and Digital PCR. *SLAS Technol.* **2017**, *22* (4), 369−386.

(2) Basu, A. S. Digital Assays Part II: Digital Protein and Cell Assays. *SLAS Technol.* **2017**, *22* (4), 387−405.

(3) Rissin, D. M.; Kan, C. W.; Campbell, T. G.; Howes, S. C.; Fournier, D. R.; Song, L.; Piech, T.; Patel, P. P.; Chang, L.; Rivnak, A. J.; Ferrell, E. P.; Randall, J. D.; Provuncher, G. K.; Walt, D. R.; Duffy, D. C. Single-Molecule Enzyme-Linked Immunosorbent Assay Detects Serum Proteins at Subfemtomolar Concentrations. *Nat. Biotechnol.* **2010**, *28*, 595.

(4) Yelleswarapu, V.; Buser, J. R.; Haber, M.; Baron, J.; Inapuri, E.; Issadore, D. Mobile Platform for Rapid Sub-Picogram-per-Milliliter, Multiplexed, Digital Droplet Detection of Proteins. *Proc. Natl. Acad. Sci. U. S. A.* **2019**, *116* (10), 4489.

(5) Rondelez, Y.; Tresset, G.; Tabata, K. V.; Arata, H.; Fujita, H.; Takeuchi, S.; Noji, H. Microfabricated Arrays of Femtoliter Chambers Allow Single Molecule Enzymology. *Nat. Biotechnol.* **2005**, *23*, 361−365.

(6) Gruner, P.; Riechers, B.; Semin, B.; Lim, J.; Johnston, A.; Short, K.; Baret, J.-C. Controlling Molecular Transport in Minimal Emulsions. *Nat. Commun.* **2016**, *7* (1), 10392.
(7) Wu, C. Y.; Ouyang, M.; Wang, B.; de Rutte, J.; Joo, A.; Jacobs, M.; Ha, K.; Bertozzi, A. L.; di Carlo, D. Monodisperse Drops Templated by 3D-Structured Microparticles. *Sci. Adv.* **2020**, *6* (45), eabb9023.
(8) Destgeer, G.; Ouyang, M.; Wu, C.-Y.; di Carlo, D. Fabrication of 3D Concentric Amphiphilic Microparticles to Form Uniform Nanoliter Reaction Volumes for Amplified Affinity Assays. *Lab Chip* **2020**, *20* (19), 3503−3514.
(9) Leigh, J. A.; Alvarez, M.; Rodriguez, C. J. Ethnic Minorities and Coronary Heart Disease: An Update and Future Directions. *Curr. Atheroscler. Rep.* **2016**, *18* (2), 9.
(10) Benjamin, E. J.; Muntner, P.; Alonso, A.; Bittencourt, M. S.; Callaway, C. W.; Carson, A. P.; Chamberlain, A. M.; Chang, A. R.; Cheng, S.; Das, S. R.; Delling, F. N.; Djousse, L.; Elkind, M. S. V.; Ferguson, J. F.; Fornage, M.; Jordan, L. C.; Khan, S. S.; Kissela, B. M.; Knutson, K. L.; Kwan, T. W.; et al. Heart Disease and Stroke Statistics—2019 Update: A Report From the American Heart Association. *Circulation* **2019**, *139* (10), No. e56-e528.
(11) Mozaffarian, D.; Benjamin, E. J.; Go, A. S.; Arnett, D. K.; Blaha, M. J.; Cushman, M.; De Ferranti, S.; Després, J. P.; Fullerton, H. J.; Howard, V. J.; Huffman, M. D.; Judd, S. E.; Kissela, B. M.; Lackland, D. T.; Lichtman, J. H.; Lisabeth, L. D.; Liu, S.; Mackey, R. H.; Matchar, D. B.; McGuire, D. K.; et al. Heart Disease and Stroke Statistics—2015 Update. *Circulation* **2015**, *131* (4), No. e29-e39.
(12) Virani, S. S.; Alonso, A.; Aparicio, H. J.; Benjamin, E. J.; Bittencourt, M. S.; Callaway, C. W.; Carson, A. P.; Chamberlain, A. M.; Cheng, S.; Delling, F. N.; Elkind, M. S. V.; Evenson, K. R.; Ferguson, J. F.; Gupta, D. K.; Khan, S. S.; Kissela, B. M.; Knutson, K. L.; Lee, C. D.; Lewis, T. T.; Liu, J.; et al. Heart Disease and Stroke Statistics—2021 Update. *Circulation* **2021**, *143* (8), E254−E743.
(13) Bahrami, H.; Kronmal, R.; Bluemke, D. A.; Olson, J.; Shea, S.; Liu, K.; Burke, G. L.; Lima, J. A. C. Differences in the Incidence of Congestive Heart Failure by Ethnicity: The Multi-Ethnic Study of Atherosclerosis. *Arch Intern Med.* **2008**, *168* (19), 2138−2145.
(14) Taylor, C. J.; Hartshorne-Evans, N.; Satchithananda, D.; Hobbs, F. D. R. FASTer Diagnosis: Time to BEAT Heart Failure. *BJGP Open* **2021**, *5* (3), BJGPO.2021.0006.
(15) Yancy, C. W.; Jessup, M.; Bozkurt, B.; Butler, J.; Casey, D. E.; Colvin, M. M.; Drazner, M. H.; Filippatos, G. S.; Fonarow, G. C.; Givertz, M. M.; Hollenberg, S. M.; Lindenfeld, J. A.; Masoudi, F. A.; McBride, P. E.; Peterson, P. N.; Stevenson, L. W.; Westlake, C. 2017 ACC/AHA/HFSA Focused Update of the 2013 ACCF/AHA Guideline for the Management of Heart Failure: A Report of the American College of Cardiology/American Heart Association Task Force on Clinical Practice Guidelines and the Heart Failure Society of America. *J. Am. Coll Cardiol* **2017**, *70* (6), 776−803.
(16) Maisel, A.; Barnard, D.; Jaski, B.; Frivold, G.; Marais, J.; Azer, M.; Miyamoto, M. I.; Lombardo, D.; Kelsay, D.; Borden, K.; Iqbal, N.; Taub, P. R.; Kupfer, K.; Clopton, P.; Greenberg, B. Primary Results of the HABIT Trial (Heart Failure Assessment With BNP in the Home). *J. Am. Coll Cardiol* **2013**, *61* (16), 1726−1735.
(17) Destgeer, G.; Ouyang, M.; Di Carlo, D. Engineering Design of Concentric Amphiphilic Microparticles for Spontaneous Formation of Picoliter to Nanoliter Droplet Volumes. *Anal. Chem.* **2021**, *93* (4), 2317−2326.
(18) Sahin, M. A.; Werner, H.; Udani, S.; Di Carlo, D.; Destgeer, G. Flow Lithography for Structured Microparticles: Fundamentals, Methods and Applications. *Lab Chip* **2022**, *22* (21), 4007−4042.
(19) Ouyang, M.; di Carlo, D. Nanoplasmonic Swarm Biosensing Using Single Nanoparticle Colorimetry. *Biosens Bioelectron* **2019**, *132*, 162−170.
(20) Ponikowski, P.; Voors, A. A.; Anker, S. D.; Bueno, H.; Cleland, J. G. F.; Coats, A. J. S.; Falk, V.; González-Juanatey, J. R.; Harjola, V.-P.; Jankowska, E. A.; Jessup, M.; Linde, C.; Nihoyannopoulos, P.; Parissis, J. T.; Pieske, B.; Riley, J. P.; Rosano, G. M. C.; Ruilope, L. M.; Ruschitzka, F.; Rutten, F. H.; van der Meer, P.; et al. 2016 ESC Guidelines for the Diagnosis and Treatment of Acute and Chronic Heart FailureThe Task Force for the Diagnosis and Treatment of Acute and Chronic Heart Failure of the European Society of Cardiology (ESC)Developed with the Special Contribution of the Heart Failure Association (HFA) of the ESC. *Eur. Heart J.* **2016**, *37* (27), 2129−2200.
(21) Chow, S. L.; Maisel, A. S.; Anand, I.; Bozkurt, B.; de Boer, R. A.; Felker, G. M.; Fonarow, G. C.; Greenberg, B.; Januzzi, J. L.; Kiernan, M. S.; Liu, P. P.; Wang, T. J.; Yancy, C. W.; Zile, M. R. Role of Biomarkers for the Prevention, Assessment, and Management of Heart Failure: A Scientific Statement From the American Heart Association. *Circulation* **2017**, *135* (22), No. e1054-e1091.
(22) Ezekowitz, J. A.; O'Meara, E.; McDonald, M. A.; Abrams, H.; Chan, M.; Ducharme, A.; Giannetti, N.; Grzeslo, A.; Hamilton, P. G.; Heckman, G. A.; Howlett, J. G.; Koshman, S. L.; Lepage, S.; McKelvie, R. S.; Moe, G. W.; Rajda, M.; Swiggum, E.; Virani, S. A.; Zieroth, S.; Al-Hesayen, A.; et al. 2017 Comprehensive Update of the Canadian Cardiovascular Society Guidelines for the Management of Heart Failure. *Canadian Journal of Cardiology* **2017**, *33* (11), 1342−1433.
(23) Reddy, B. S.; Chatterji, B. N. An FFT-Based Technique for Translation, Rotation, and Scale-Invariant Image Registration. *IEEE Trans. on Image Process.* **1996**, *5* (8), 1266−1271.
(24) Robertson, M. A.; Borman, S.; Stevenson, R. L. Dynamic Range Improvement through Multiple Exposures. *Proc. 1999 IEEE Int. Conf. Image Process.* **1999**, *3*, 159−163.
(25) Reddy, B.S.; Chatterji, B.N. An FFT-Based Technique for Translation, Rotation, and Scale-Invariant Image Registration. *IEEE Trans. on Image Process.* **1996**, *5* (8), 1266−1271.
(26) Zuiderveld, K. Contrast Limited Adaptive Histogram Equalization. *Graphics Gems* **1994**, 474−485.
(27) Tomasi, C.; Manduchi, R. Bilateral Filtering for Gray and Color Images. *Proc. IEEE Int. Conf. Comput. Vision* **1998**, 839−846.
(28) Canny, J. A Computational Approach to Edge Detection. *IEEE Trans. Pattern Anal. Mach. Intell.* **1986**, *PAMI-8* (6), 679.

https://doi.org/10.1021/acsnano.3c04994
ACS Nano 2023, 17, 19952−19960